



1 **Mercury distribution and transport in the North Atlantic Ocean along**  
2 **the GEOTRACES-GA01 transect**

3  
4 Daniel Cossa<sup>1</sup>, Lars-Eric Heimbürger<sup>2</sup>, Fiz F. Pérez<sup>3</sup>, Maribel I. García-Ibáñez<sup>3</sup>, Jeroen  
5 E. Sonke<sup>4</sup>, H el ene Planquette<sup>5</sup>, Pascale Lherminier<sup>6</sup>, G eraldine Sarthou<sup>5</sup>

6  
7 <sup>1</sup>ISTerre, Universit e Grenoble Alpes, CS 40700, F-38058 Grenoble Cedex 9, France

8 <sup>2</sup>Aix Marseille Universit e, CNRS/INSU, Universit e de Toulon, IRD, Mediterranean Institute of  
9 Oceanography (MIO) UM 110, Marseille, France

10 <sup>3</sup>Instituto de Investigaciones Marinas, CSIC, Eduardo Cabello 6, E-36208 Vigo, Spain

11 <sup>4</sup>CNRS, GET-OMP, 14 Ave. E. Belin, F-31240 Toulouse, France

12 <sup>5</sup>LEMAR, Universit e de Bretagne Occidentale, F-29280 Plouzan e, France

13 <sup>6</sup>IFREMER, Brittany Center, LPO, BP 70, F-29280 Plouzan e, France

14

15 **Abstract**

16 We report here the results of total mercury (HgT) determinations along the 2014  
17 GEOTRACES GEOVIDE cruise (GA01 transect) in the North Atlantic Ocean (NA) from  
18 Lisbon (Portugal) to the Labrador coast (Canada). Ninety-seven percent of the HgT  
19 concentrations of unfiltered samples (HgT<sub>UNF</sub>) ranged between 0.16 and 1.00 pmol L<sup>-1</sup>.  
20 The geometric mean was 0.51 pmol L<sup>-1</sup> for the 535 samples analysed. The dissolved  
21 fraction (< 0.45 µm) of HgT, determined on 141 samples, averaged 78 % of the HgT<sub>UNF</sub>  
22 for the whole water column. HgT<sub>UNF</sub> concentrations increased eastwards and with depth  
23 from Greenland to Europe and from sub-surface to bottom waters, respectively. The Hg  
24 distribution mirrored that of dissolved oxygen concentration, with highest HgT<sub>UNF</sub>  
25 levels associated with oxygen-depleted zones. The statistically significant (p < 0.01)  
26 relationship between HgT<sub>F</sub> (filtered samples) and the apparent oxygen utilization  
27 confirms the nutrient-like behavior of Hg in the NA. An extended Optimum  
28 Multiparameter Analysis allowed us to characterize HgT<sub>UNF</sub> concentrations in the  
29 different Source Water Types (SWTs) present along the transect. Mean HgT<sub>UNF</sub>  
30 concentrations ranged from 0.26 ± 0.03 pmol L<sup>-1</sup> in the Irminger Subpolar Mode Water



31 to  $1.02 \pm 0.02$  pmol L<sup>-1</sup> in the lower North East Atlantic Deep Water. Anthropogenic  
32 Hg-enriched SWTs were found in the upper oceanic layers (i.e., East North Atlantic  
33 Central Water and Subarctic Intermediate Water). The change in anthropogenic Hg  
34 concentrations in the Labrador Sea Water, during its eastward journey, suggests a  
35 continuous decrease of Hg content in this water mass over the last decades. Calculation  
36 of the water transport driven by the Atlantic Meridional Overturning Circulation across  
37 the Portugal-Greenland transect indicates a northward Hg transport within the upper  
38 limb, and a southward Hg transport within the lower limb, with a resulting net transport  
39 from low latitudes to the polar zones of about 111 kmol yr<sup>-1</sup>.

40

## 41 **1. Introduction**

42 Many trace elements have a physiological function for marine phytoplankton (e.g.,  
43 Morel et al., 2003). Others, such as mercury (Hg), have no known beneficial role for  
44 most of biological systems, and may even provoke toxicological disturbances of marine  
45 ecosystems (e.g., Fitzgerald et al., 2007; Mason et al., 2012). The global Hg  
46 biogeochemical cycle is dominated by the atmosphere-ocean exchanges, with  
47 atmospheric Hg deposition representing the principal source of inorganic Hg to the open  
48 ocean (e.g., Mason et al., 2012; Sonke et al., 2013). Once deposited at the ocean surface,  
49 Hg penetrates the ocean interior both *via* water mass formation, i.e., sinking of surface  
50 waters to depth (the solubility pump), and *via* Hg sorption, sinking, and subsequent  
51 remineralization of biogenic particles produced in the euphotic zone (the biological  
52 pump) at depth. Anthropogenic Hg emissions to the atmosphere have severely altered  
53 the Hg cycle during the last centuries (e.g., Fitzgerald et al., 2007; Lamborg et al.,



54 2014). Modern Hg concentrations in the global atmosphere are more than three times  
55 the pre-industrial Hg concentrations, leading to a doubling of the Hg concentrations in  
56 surface ocean (Mason et al., 2012; Lamborg et al., 2014; Amos et al., 2015).  
57 Recognizing the toxicological potential of this Hg anthropization of the oceans, national  
58 and international agencies have proposed and enforced regulations since the 1980s to  
59 reduce man-made Hg emissions to the environment (Pirrone and Mahaffey, 2005). For  
60 this purpose, United Nation Environment Program led to the adoption of the Minamata  
61 Convention (UNEP, 2013). Within this context, it is important to characterize the Hg  
62 content of various water masses of the Global Ocean and to monitor their temporal  
63 variations.

64 The North Atlantic Ocean (NA) is one of the places where deep water formation  
65 (e.g., Labrador Sea Water, LSW) is particularly important and, thus, where atmospheric  
66 Hg deposition can enter into the ocean interior *via* the solubility pump, offering a  
67 unique opportunity for studying the oceanic response to changes in atmospheric Hg  
68 inputs. In addition, recent improvements in the precision and accuracy of total mercury  
69 (HgT) analyses allowed a more detailed description of the NA HgT distribution,  
70 especially within the GEOTRACES program (e.g., Cossa et al., 2011; Lamborg et al.,  
71 2014; Bowman et al., 2015; Munson et al., 2015). New GEOTRACES results provide  
72 evidence that the main features of the HgT distribution patterns are related to the  
73 physical and biogeochemical oceanographic properties of waters masses. In the NA, the  
74 GEOTRACES-GA03 zonal and meridional transects, sampled in 2010 and 2011, covered  
75 the NA from East to West between 18°N and 40°N, from Africa to USA coasts. Here,  
76 we report the results of the GEOVIDE cruise, along the GEOTRACES-GA01 transect,



77 which targeted the NA from 40°N to 60°N, from Portugal to Newfoundland, *via* the  
78 southern tip of Greenland (Fig. 1).

79 This article provides (i) a high-resolution description of the HgT distribution in  
80 the waters of Subpolar and Subtropical gyres of the NA, (ii) a characterization the HgT  
81 concentrations of the main water masses of the NA, (iii) an estimate of the temporal  
82 change of anthropogenic Hg in LSW, and (iv) a quantification the HgT transport  
83 associated with the upper and lower limbs of the Atlantic Meridional Overturning  
84 Circulation (AMOC).

85

## 86 2. Oceanographic context

87 A full description of the water masses along the GEOTRACES-GA01 transect can be  
88 found in García-Ibáñez et al. (this issue). Briefly, the North Atlantic Current (NAC)  
89 conveys the warm salty surface waters from subtropical regions northwards to the  
90 subpolar regions, where they are cooled down by heat exchange with the atmosphere  
91 (Fig. 1). The intermediate and deep waters formed this way fill up the Global Ocean,  
92 initiating the southward-flowing limb of the AMOC (e.g., McCartney and Talley, 1984;  
93 Lherminier et al., 2010). In addition, the general circulation pattern is characterized by  
94 the subtropical and the subpolar gyres (Fig. 1).

95 In the Subtropical Gyre (Fig. 1), several water masses are stacked up from surface  
96 to bottom: (i) the mixed layer, (ii) the East North Atlantic Central Water (ENACW),  
97 (iii) the Mediterranean Water (MW), (iv) the Labrador Sea Water (LSW) and (v) the  
98 lower North East Atlantic Deep Water (NEADW<sub>L</sub>), which contains about 30%



99 Antarctic Bottom Water (AABW) (García-Ibáñez et al., 2015). The transformation of  
100 ENACW leads to the formation of different mode waters including the Subpolar Mode  
101 Waters (SPMWs) (McCartney and Talley, 1982; Tsuchiya et al., 1992; van Aken and  
102 Becker, 1996; Brambilla and Talley, 2008; Cianca et al., 2009). SPMWs are the near-  
103 surface water masses of the Subpolar Gyre of the NA characterized by thick layers of  
104 nearly uniform temperature, often defined as SPMW with a temperature as a subscript  
105 (SPMW<sub>8</sub> for example). SPMWs are formed during winter convection at high latitude,  
106 due to atmospheric freshening of surface waters originating from the subtropical gyre  
107 (McCartney, 1992). SPMWs participate in the upper limb of the AMOC and provide  
108 much of the water that is eventually transformed into the several components of North  
109 Atlantic Deep Water (NADW; Brambilla and Talley, 2008).

110 In the Subpolar Gyre, ocean-atmosphere interaction is particularly intense. The  
111 cooling down of subtropical waters produces dense waters, triggering the deepening of  
112 the mixed layer and further leading to deep convection. The main NA convection zones  
113 are located in the Labrador (LS), Irminger (IrS) and Nordic seas (NS) (Fig. 1).  
114 Convection in those zones leads to the formation of intermediate and deep waters such  
115 as LSW, Denmark Strait Overflow Water (DSOW) and Iceland-Scotland Overflow  
116 Water (ISOW). LSW and ISOW are the main components of NEADW, and the all three  
117 are the components of the NADW, which constitutes the cold deep southward-flowing  
118 limb of the AMOC, flowing towards the Southern Ocean in the western Atlantic basin.  
119 LSW has been variably produced in the past fifty years depending on the intensity of  
120 winter convection, linked to the intensity of the North Atlantic Oscillation (e.g., Rhein  
121 et al., 2002; Cianca et al., 2009; Yashayaev and Loder, 2016). Depths of winter



122 convection in the LS vary from a few hundred meters (the early 2000s) to over 2000 m  
123 (early 1990s). The LSW is a thick layer in the LS and thins out as it travels  
124 southwestwardly. It spreads out into the entire NA, filling the Subpolar Gyre and  
125 entering the Subtropical Gyre. Within the Subpolar Gyre, LSW is marked by a salinity  
126 minimum above the ISOW. In both gyres, the well-ventilated LSW is noticeable by a  
127 marked oxygen maximum.

128 In the deep convection zones, atmospheric compounds, including those of volatile  
129 chemicals such as chlorofluorocarbons (CFCs) (Smethie et al., 2000) are injected into  
130 the ocean interior. In the Eastern NA, very low CFC concentrations below LSW  
131 characterize the NEADW<sub>L</sub> and attest of negligible atmospheric exchange (McCartney  
132 and Talley, 1984; Rhein et al., 2002). Hg partly follows the pathway of CFCs; it  
133 intrudes into the interior of the Atlantic Ocean through surface waters at higher latitudes  
134 in the NA and is conveyed by the AMOC. The upper part of LSW and DSOW have  
135 relatively high CFC concentrations (Azetsu-Scott et al., 2003). The CFC maximum is  
136 located between 1200 -1500 m-depth for LSW but can penetrate deeper down to 2000  
137 m-depth, and the CFC maximum for DSOW is at 3500 m (Smethie et al., 2000). Hg  
138 enters the Ocean's interior by a similar mechanism, and, in productive zones, Hg can  
139 also enter with sinking organic particles.

140

### 141 **3. Material and methods**

#### 142 **3.1. Sampling**



143 Water samples were collected during the French-led GEOVIDE cruise (GEOTRACES-  
144 GA01 transect), on board the RV *Pourquoi Pas?* sailing from Lisbon (Portugal) on May  
145 15<sup>th</sup> to arrive on June the 30<sup>th</sup> 2014 in St John's (Newfoundland, Canada) (Fig. 1).  
146 Seventy-eight (78) stations (Table S1) were occupied for hydrographic profiles (CTD,  
147 dissolved oxygen, nutrients, etc.), among which 29 included trace metal sampling.  
148 Sampling and water treatment for HgT determination (Lamborg et al., 2012; Cutter et  
149 al., 2017) were performed using ultra-trace techniques following the GEOTRACES  
150 recommendations. During the GEOVIDE cruise, an epoxy-coated aluminum rosette,  
151 equipped with 12 L GO-FLO (General Oceanics®) bottles initially cleaned following the  
152 GEOTRACES procedures (Cutter and Bruland, 2012), was deployed on a 6 mm Kevlar  
153 hydrowire. The rosette was also equipped with probes for pressure, conductivity,  
154 temperature, dissolved oxygen, fluorometry and transmission measurements (titanium  
155 SBE model 911-plus, Sea-Bird Electronics®). Specifically, for Hg determination, all  
156 material in contact with the seawater samples was made of Teflon or Teflon coated, acid  
157 cleaned and rinsed with ultrapure water (Milli-Q, Millipore®) prior to utilization.  
158 Original vent fixture and sampling valves of the GO-FLO bottles were replaced with  
159 Teflon (PTFE) ones. GO-FLO bottles were sub-sampled under a laminar flow bench  
160 inside a trace metal clean container. The efficiency of the High-Efficiency Particulate  
161 Air filter (HEPA, 0.3 µm) in the container was checked with a Coulter Counter during  
162 the cruise. All subsequent sample treatments (including filtration) and Hg analyses were  
163 also performed in class 100 clean containers. For sample filtrations, acid-washed 0.45  
164 µm polycarbonate membranes (Nuclepore) were preferred to cellulose acetate or  
165 polyethersulfone membranes proposed in the GEOTRACES protocols (Fig. S1). Sub-



166 samples were stored in Teflon bottles (FEP) until the on board HgT analyses, which  
167 occurred within 6 hours after sampling.

### 168 **3.2. Chemical analyses**

169 In order to access all Hg species, the release of Hg from its ligands was achieved by a  
170 BrCl solution (50  $\mu$ L of a 0.2 N solution is added to a 40-mL sample), and then the Hg  
171 was reduced with an acidic SnCl<sub>2</sub> solution (100  $\mu$ L of a 1 M solution is added to a 40-  
172 mL sample). Potassium bromide (Sigma Aldrich, USA) and potassium bromate (Sigma  
173 Aldrich, USA) were heated for 4 h at 250°C to remove Hg traces before making up  
174 BrCl solution with freshly double-distilled HCl (Heimbürger et al., 2015). The  
175 generated Hg vapor was amalgamated on a gold trap and then released by heating into  
176 an atomic fluorescence spectrometer (AFS). We used two AFS systems in parallel  
177 (Tekran® Model 2500, Brooks® Model 3), both calibrated against the NIST 3133  
178 certified reference material. This technique, initially described by Bloom and Crecelius  
179 (1983) and subsequently improved by Gill and Fitzgerald (1985), is now an  
180 authoritative procedure officialised by the US-EPA as method 1631 (EPA, 2002). The  
181 definitions of detection limit (DL), reproducibility and accuracy given here are adopted  
182 from Taylor (1987) and Hewitt (1989). Using a mirrored quartz cuvette (Hellma®)  
183 allowed for an “absolute DL”, defined as two times the electronic noise magnitude, as  
184 low as 1.7 femtomoles. However, in practice for trace measurements, the DL is  
185 governed by the reproducibility of the blank values, and calculated as 3.3 times the  
186 standard deviation of blank values. The blank was determined on a purged Hg-free  
187 seawater sample spiked with reagents (i.e., BrCl and SnCl<sub>2</sub>). The mean ( $\pm$  standard  
188 deviation) of blanks measured during the GEOVIDE cruise was  $3.2 \pm 1.0$  femtomoles.



189 Thus, for a 40-mL seawater aliquot, the DL expressed in HgT concentration was 0.07  
190 pmol L<sup>-1</sup>. The reproducibility (coefficient of variation of six replicate measures) varied  
191 according to the concentration level between 5 and 15 %. The accuracy of HgT  
192 measurements was tested using ORMS-5 certified reference material (CRM) from the  
193 National Research Council of Canada (<http://www.nrc-cnrc.gc.ca/>), as spike addition to  
194 a purged Hg-free seawater sample. Measurements were always within the given  
195 confidence interval. To ensure good data quality, and as a continuity of previous efforts  
196 (Cossa and Courau, 1990; Lamborg et al., 2012), we organized the 2014 GEOTRACES  
197 intercalibration exercise for total HgT and methyl Hg as a part of the GEOVIDE cruise.  
198 The intercalibration sample was taken on June 22<sup>nd</sup>, 2014 in the LS at 49.093°W,  
199 55.842°N, and 2365 m-depth. The sample was sent out to 10 participating laboratories.  
200 This station was also planned as crossover station within the 2015 Arctic GEOTRACES  
201 effort (Canadian cruise) but has been changed subsequently to another location. Our  
202 results compare well with the consensus values, HgT = 0.63 ± 0.12 pmol L<sup>-1</sup>, n = 8. We  
203 measured the 2014 GEOTRACES intercalibration sample twice for HgT and obtained 0.51  
204 (22<sup>nd</sup> June 2014, on board) and 0.58 pmol L<sup>-1</sup> (30<sup>th</sup> October 2014, home lab).

### 205 **3.3. *Extended Optimum Multiparameter analysis***

206 We used an extended Optimum Multiparameter (eOMP) analysis to characterize the  
207 water mass HgT<sub>UNF</sub> concentrations along the GEOTRACES-GA01 transect (García-Ibáñez  
208 et al., 2015, this issue). The eOMP analysis quantifies the proportions of the different  
209 Source Water Types (SWTs) that contribute to a given water sample. The HgT<sub>UNF</sub>  
210 concentration of each SWT, [HgT<sub>UNF</sub>]<sub>i</sub>, was estimated through an inversion of the SWT  
211 fractions given by the eOMP analysis. Such an approach was successfully applied to



212 dissolved-organic-carbon water mass definitions in the NA (Fontela et al., 2016) and for  
213 evaluating the impact of water mass mixing and remineralization on the N<sub>2</sub>O  
214 distribution in the NA (de la Paz et al., 2017). Here, we performed an inversion of a  
215 system of 430 equations (HgT<sub>UNF</sub> samples) and 11 unknowns ([HgT<sub>UNF</sub>]<sub>i</sub>). Samples for  
216 which the difference between the observed HgT<sub>UNF</sub> and the predicted HgT<sub>UNF</sub> values by  
217 the multiple linear regression (Eq. 1 below) was three times greater than the standard  
218 deviation were removed from the analysis. Nine samples were concerned: Sta. 2 (125  
219 m), Sta. 11 (793 m), Sta. 11 (5242 m), Sta. 13 (1186 m), Sta. 15 (170 m), Sta. 19 (99  
220 m), Sta. 26 (97 m), Sta. 32 (596 m), and Sta. 38 (297 m). The SWTs were characterized  
221 by potential temperature, salinity, and macronutrients. The eOMP was restricted to  
222 depths below 75 m in order to avoid air-sea interaction effects. The eOMP gave us the  
223 fractions of the 11 SWTs, and we resolved the following expression to estimate the  
224 [HgT<sub>UNF</sub>]<sub>i</sub>:

$$225 \quad [HgT_{UNF}]_j = \sum_{i=1}^{11} SWT_i^j * [HgT_{UNF}]_i + \epsilon_j \quad (j = 1 \dots 430) \quad (1)$$

226 where [HgT<sub>UNF</sub>]<sub>j</sub> represents the measured HgT<sub>UNF</sub> concentration for each sample “j”,

227  $SWT_i^j$  the proportion of SWT “i” to sample “j” (obtained through the eOMP),

228 [HgT<sub>UNF</sub>]<sub>i</sub> the HgT<sub>UNF</sub> concentration for each SWT “i” (unknown), and  $\epsilon_j$  the residual.

229 The 430  $\epsilon_j$ s of the inversion presented a null mean and a standard deviation of 0.085

230 pmol L<sup>-1</sup> (R = 0.84).

### 231 3.4. Mercury transport calculation

232 Velocity fields across the GEOTRACES-GA01 transect were calculated using inverse

233 model constrained by Doppler current profiler velocity measurements (Zunino et al.,



234 this issue) an overall mass balance of  $1 \pm 3$  Sv to the North (Lherminier et al., 2007,  
235 2010). The volume transport per SWT was computed by combining these velocity fields  
236 with the results of the eOMP (García-Ibáñez et al., this issue). Finally, the  $HgT_{UNF}$   
237 transports per water mass were calculated through Eq. (2):

$$238 \quad 4. \quad T_{HgT_{UNF}} = \sum_{i=1}^{11} T_{SWT_i} * [HgT_{UNF}]_i * \rho_i \quad (2)$$

239 where  $T_{SWT_i}$  is the volume transport of SWT “*i*”,  $[HgT_{UNF}]_i$  is the  $HgT_{UNF}$  concentration  
240 for each SWT “*i*” (from Eq. 1), and  $\rho_i$  is the density of the SWT “*i*”.

241 The inverse model configuration for the GEOVIDE cruise data is described in Zunino et  
242 al. (this issue). The inverse model is based on the least-squares formalism, which  
243 provides errors on the velocities and associated quantities such as the magnitude of the  
244 AMOC (estimated in density coordinate) and the heat flux (Lherminier et al., 2010).  
245 The inverse model computes the absolute geostrophic transports orthogonal to the  
246 section. The Ekman transport is deduced from the wind fields averaged over the cruise  
247 period and added homogeneously in the upper 40 m (Mercier et al., 2015). The transport  
248 estimates of the inverse model across the section have been validated by favorable  
249 comparisons with independent measurements (Gourcuff et al., 2011; Daniault et al.,  
250 2011; Mercier et al., 2015).

251

## 252 **5. Results**

253  $HgT_{UNF}$  concentrations along the GEOTRACES-GA01 transect ranged from 0.16 to 1.54  
254  $\text{pmol L}^{-1}$  ( $n = 535$ ), these data being log-normally distributed, positively skewed  
255 (Skewness = 1.1; Kurtosis = 2.1; Fig. S2) and with 97 % of the values lower than 1.00



256 pmol L<sup>-1</sup>. The geometric mean and the median were 0.51 pmol L<sup>-1</sup>, whereas the  
257 arithmetic mean and standard deviation were 0.54 and 0.19 pmol L<sup>-1</sup>, respectively.  
258 These concentrations are within the range found along the GEOTRACES-GA03 transect  
259 (0.09–1.89 pmol L<sup>-1</sup>, n = 605) that crossed the NA within the subtropical gyre from  
260 18°N to 40°N (Bowman et al., 2015), but lower than the range and the unusually high  
261 arithmetic mean determined in the South Atlantic along the GEOTRACES-GA10 transect  
262 (0.39–3.39 pmol L<sup>-1</sup>, n = 375; Bratkič, personal communication, and 1.45 ± 0.6 pmol L<sup>-1</sup>;  
263 Bratkič et al., 2016, respectively).

264 The overall distribution of the HgT<sub>UNF</sub> concentrations along the GEOTRACES-  
265 GA01 transect is represented in Fig. 2. The main feature of HgT<sub>UNF</sub> concentrations is an  
266 eastward increase, from Greenland to Europe, and downward increase, from sub-surface  
267 to bottom waters. In addition, highest and lowest (most variable) HgT<sub>UNF</sub> values were  
268 encountered in surface/sub-surface waters, where Hg evasion to the atmosphere and  
269 high particulate matter concentrations may generate low and high HgT<sub>UNF</sub>  
270 concentrations, respectively. Out of the 141 filtered samples that were analysed,  
271 altogether, the filtered fraction of Hg (HgT<sub>F</sub>) represents, on average, 78% (range: 36–  
272 98%) of the HgT<sub>UNF</sub> (Fig. 3). Excluding the upper 100 m, where most of the particles  
273 were present, the HgT<sub>F</sub> fraction represents, on average, 81% (range: 63–98%) of the  
274 HgT<sub>UNF</sub>. In the following sub-sections, detailed descriptions of the HgT<sub>UNF</sub> profiles for  
275 the five following oceanographic environments are given: LS, IrS, Iceland basin (IcB),  
276 Eastern North Atlantic basin (ENAB) and Iberian abyssal plain (IAP).

### 277 5.1. Labrador Sea (Stas. 61 to 78)



278 In the LS, the  $\text{HgT}_{\text{UNF}}$  concentrations ranged from 0.25 to 0.67  $\text{pmol L}^{-1}$ , with a mean of  
279  $0.44 \pm 0.10 \text{ pmol L}^{-1}$  ( $n = 113$ ,  $1\sigma$ ). Distribution, source, and cycling of Hg in the LS  
280 have been described and discussed in detail in a companion paper (Cossa et al., in  
281 press). In summary: high  $\text{HgT}_{\text{UNF}}$  concentrations were found in the waters of the  
282 Labrador Current (LC) receiving freshwaters from the Canadian Arctic Archipelago,  
283 and in the waters over the Labrador shelf and rise. In the LSW formed during the 2014  
284 winter convection,  $\text{HgT}_{\text{UNF}}$  concentrations were low ( $0.38 \pm 0.05 \text{ pmol L}^{-1}$ ,  $n = 23$ ) and  
285 increased gradually with depth (up to  $> 0.5 \text{ pmol L}^{-1}$ ) in the Northeast Atlantic Deep  
286 Waters.

### 287 **5.2. Irminger Sea (Stas. 40–60)**

288  $\text{HgT}_{\text{UNF}}$  concentrations in the IrS waters varied from 0.22 to 0.76  $\text{pmol L}^{-1}$ , with a mean  
289 of  $0.45 \pm 0.10 \text{ pmol L}^{-1}$  ( $n = 103$ ). In the IrSPMW, which was encountered in the  
290 upper 1000 m near the East Greenland and the upper 500 m in the rest of the IrS (Fig. 4a  
291 in García-Ibáñez et al., this issue),  $\text{HgT}_{\text{UNF}}$  values span between 0.29 and 0.42  $\text{pmol L}^{-1}$   
292 (Fig. 2). Deeper,  $\text{HgT}_{\text{UNF}}$  increased up to 0.50 and 63  $\text{pmol L}^{-1}$  in LSW ( $\sim 1000 \text{ m}$ ) and  
293 ISOW ( $\sim 2500 \text{ m}$ ), respectively. Lower  $\text{HgT}_{\text{UNF}}$  concentrations ( $0.40\text{--}0.50 \text{ pmol L}^{-1}$ )  
294 were associated with DSOW in the very bottom waters (Sta. 42-44, Fig. 2).

### 295 **5.3. Iceland Basin (Stas. 34–38)**

296  $\text{HgT}_{\text{UNF}}$  concentrations in the IcB ranged from 0.18 to 0.65  $\text{pmol L}^{-1}$ , with a mean of  
297  $0.46 \pm 0.10 \text{ pmol L}^{-1}$  ( $n = 51$ ). In the top 100 m of the water column,  $\text{HgT}_{\text{UNF}}$   
298 concentrations were quite variable ( $0.25\text{--}0.62 \text{ pmol L}^{-1}$ ) probably as a result of the  
299 counteracting importance of Hg evasion to the atmosphere and high particulate matter  
300 concentrations. West of the IcB (Sta. 38), contrasting  $\text{HgT}_{\text{UNF}}$  levels were found on both



301 sides at 500 m, characterized by a thermohaline gradient (Fig. 2a and b in García-Ibáñez  
302 et al., this issue). In the top waters,  $\text{HgT}_{\text{UNF}}$  levels were depleted to  $0.18 \text{ pmol L}^{-1}$ ,  
303 whereas, below 500 m, they were much higher and converge to values close to what we  
304 found, at the same depths in the adjacent IrS ( $\sim 0.60 \text{ pmol L}^{-1}$ , Sta. 40). In the bottom  
305 waters, constituted by more than 50% of ISOW (García-Ibáñez et al., this issue),  
306  $\text{HgT}_{\text{UNF}}$  concentrations reached values  $> 0.50 \text{ pmol L}^{-1}$ .

#### 307 **4.4. Eastern North Atlantic Basin (Stas. 17–32)**

308 The  $\text{HgT}_{\text{UNF}}$  concentrations in the ENAB varied from  $0.18$  to  $1.14 \text{ pmol L}^{-1}$ , with a  
309 mean of  $0.61 \pm 0.18 \text{ pmol L}^{-1}$  ( $n = 174$ ). The ENAB, also named Western European  
310 Basin, is characterized by a complex vertical stratification of the water column, and the  
311 presence of the Subarctic Front (SAF) that was located between Sta. 25 and 26 in the  
312 GEOTRACES-GA01 transect (García-Ibáñez et al. and Zunino et al., this issue). West of  
313 the SAF (Stas. 26-32), the mean  $\text{HgT}_{\text{UNF}}$  concentrations was not statistically different  
314 from that obtained for stations east of the SAF (Sta. 17-25):  $0.63 \pm 0.14 \text{ pmol L}^{-1}$  ( $n =$   
315  $64$ ) versus  $0.59 \pm 0.20 \text{ pmol L}^{-1}$  ( $n = 110$ ). The  $\text{HgT}_{\text{UNF}}$  vertical profiles at all the  
316 stations of the ENAB were characterized by a complex but reproducible pattern  
317 depicting (i) two maxima peaks (the upper at subsurface, the lower within the  
318 intermediate waters), and below, (ii) a  $\text{HgT}_{\text{UNF}}$  enhancement starting from 2500 m  
319 towards the bottom (Fig. 2). The position and intensity of the peaks vary with longitude.  
320 The upper peak, which occurs within the top 200 m, is only  $0.48 \text{ pmol L}^{-1}$  at Sta. 29, but  
321 reaches  $1.14 \text{ pmol L}^{-1}$  at Sta. 19 (Fig. 2). The vertical position of maxima of the lower  
322 peak and deepens eastwards, from 200 m down to 800 m, concurrently with an increase  
323 of its amplitude (Fig. 2). The position of the upper peaks suggests a relation with the



324 abundance of phytoplankton, whereas the position of the lower peaks, which is close to  
325 the maximum of Apparent Oxygen Utilization (AOU) that rose above  $70 \mu\text{mol L}^{-1}$  (Fig.  
326 2), suggests a dependence on the organic matter remineralization (see Discussion  
327 below). Between 1400 and 2500 m, in the layer corresponding to LSW,  $\text{HgT}_{\text{UNF}}$   
328 concentrations were quite uniform, with a mean concentration of  $0.54 \pm 0.04 \text{ pmol L}^{-1}$   
329 ( $n = 18$ ).  $\text{HgT}_{\text{UNF}}$  concentration increased from 3000 m downwards to the sea bottom,  
330 consisting of NEADWL, where it reaches 0.95, 0.97, 1.03 and  $1.13 \text{ pmol L}^{-1}$  at Sta. 21,  
331 19, 25 and 23, respectively.

#### 332 **4.5. Iberian Abyssal Plain (Stas. 1–15)**

333 In the IAP,  $\text{HgT}_{\text{UNF}}$  concentrations ranged from 0.19 to  $1.54 \text{ pmol L}^{-1}$ , with a mean of  
334  $0.69 \pm 0.23 \text{ pmol L}^{-1}$  ( $n = 94$ ). The highest  $\text{HgT}_{\text{UNF}}$  concentrations were measured in the  
335 upper 100 m near the shelf slope. At Sta. 2, the only station on the European shelf  
336 (bottom at 152 m), the  $\text{HgT}_{\text{UNF}}$  concentrations increased from 10 m to the bottom, from  
337  $0.38$  to  $0.86 \text{ pmol L}^{-1}$ , but did not differ from the open NA ocean levels. Off-shore, at  
338 Sta. 1, 11, 13 and 15 (Fig. 2), the vertical distributions of  $\text{HgT}_{\text{UNF}}$  presented a certain  
339 similarity with those of the eastern ENAB, but with an additional third deep peak. As in  
340 the eastern ENAB, the upper peak is associated with subsurface waters, and the second,  
341 centered around 800 m, is associated with the oxygen minimum of SPMW<sub>8</sub>. The third  
342 peak, centered around 1100-1200 m, is associated with the salinity maximum of the  
343 core of MW. The presence of a  $\text{HgT}_{\text{UNF}}$  peak in the MW was still visible westwards, at  
344 Sta. 17, 19 and 23, near 1100 m, as a shoulder of the main peak at 800 m (Fig. 2).  
345 Deeper in the water column,  $\text{HgT}_{\text{UNF}}$  increased gradually from 2000 m (LSW) to 3000



346 m (ISOW), 3500 m and below (NEADW<sub>L</sub>), where HgT<sub>UNF</sub> concentrations reached 0.87  
347 to 1.04 pmol L<sup>-1</sup> depending on the station.

348

## 349 5. Discussion

### 350 5.1. Biogeochemical and hydrographical controls on HgT distribution

351 Hg is dispersed in the atmosphere, deposited on sea surfaces, and drawn down to the  
352 ocean interior with downwards convecting waters, and/or associated with sinking  
353 particles. At depth, the dissolution of particulate matter, produced as a result of organic  
354 matter microbiological remineralization, remobilizes Hg from particles produced in the  
355 euphotic zone.

356 The biological pumping/regeneration process entails the existence of relationships  
357 between Hg concentrations and nutrient or dissolved oxygen concentration (or AOU),  
358 which are proxies of the organic matter remineralization (mainly the microbial  
359 respiration) that the sample has experienced since it was last in contact with the  
360 atmosphere. Such a biogeochemical behaviour, which is qualified of “nutrient-like”  
361 behaviour, is observed in the present study (Fig. 4). The correlation coefficient (R)  
362 between HgT<sub>F</sub> and the AOU, reached the highly statistically significant value of 0.87 (n  
363 = 141,  $p < 0.01$ ). Similar behaviour was already observed in the water column near the  
364 shelf edge of the western European margin (Cossa et al., 2004), and elsewhere in the  
365 NA (Lamborg et al., 2014; Bowman et al., 2015). Thus, biological uptake and  
366 regenerative processes appear to control the oceanic Hg distribution in the Subpolar and  
367 Subtropical gyres of the NA.



368 Hydrological circulation impacts the Hg distribution in the NA. We estimated the  
369  $\text{HgT}_{\text{UNF}}$  (and AOU) values of each SWT using eOMP (Table 1). The correlation  
370 coefficient between observed and predicted (eOMP-based) values through Eq. (1)  
371 (Material and Methods section) for  $\text{HgT}_{\text{UNF}}$  is 0.71. The estimated  $\text{HgT}_{\text{UNF}}$   
372 concentrations vary significantly between SWTs (ANOVA,  $p < 0.01$ ), from  $0.26 \pm 0.03$   
373 to  $1.02 \pm 0.02 \text{ pmol L}^{-1}$ , for the IrSPM to the NEADW<sub>L</sub>, respectively. The low  $\text{HgT}_{\text{UNF}}$   
374 value in the IrSPMW, the youngest SPMW formed in the IrS as a result of air-sea  
375 interaction of the waters transported northwards by the NAC (e.g., McCartney and  
376 Talley, 1984), is similar to that found in the LSW formed during the 2014-winter  
377 convection in the LS (Cossa et al., in press), consistently with hydrographic features,  
378 which suggests that the IrSPMW is a precursor of LSW formed in the LS (Pickart et al.,  
379 2003). The highest estimated  $\text{HgT}_{\text{UNF}}$  concentration is calculated for NEADW<sub>L</sub>, which  
380 is the dominant water mass in the bottom IAP, with its main core below ~3500 m-depth  
381 and spreading down to the bottom (García-Ibáñez et al., this issue), where it mixes with  
382 the Hg-rich AABW, a deep-water mass originating from the Southern Ocean ( $\text{HgT}_{\text{AABW}}$   
383 =  $1.35 \pm 0.39 \text{ pmol L}^{-1}$ , Cossa et al., 2011). Thus, both AABW influence and organic  
384 matter remineralization (AOU ~99  $\mu\text{mol L}^{-1}$ , Table 1) converge to explain the Hg-  
385 enrichment of NEADW<sub>L</sub>. The same rationale can be drawn for the estimated  $\text{HgT}_{\text{UNF}}$   
386 concentration in MW ( $0.75 \pm 0.04 \text{ pmol L}^{-1}$ , Table 1). MW originating from the  
387 Mediterranean Sea is located just below SPMW<sub>8</sub>, with a core at 1100 m (García-Ibáñez  
388 et al., this issue). Both SPMW<sub>8</sub> and MW are characterized by elevated  $\text{HgT}_{\text{UNF}}$   
389 concentration and AOU values (see eOMP estimates in Table 1). Indeed, recent  
390 measurements in the waters of the Western Mediterranean state  $\text{HgT}_{\text{UNF}}$  values varying



391 between 0.53 and 1.25 pmol L<sup>-1</sup> within the layer that flows out of the Mediterranean Sea  
392 at the Strait of Gibraltar (Cossa and Coquery, 2005; Cossa et al., 2017). In addition,  
393 PIW and SPMW<sub>8</sub>, present also relatively high HgT<sub>UNF</sub> and AOU concentrations (Table  
394 1).

395 In order to sort out the influence of remineralization processes on the HgT<sub>UNF</sub> in  
396 each SWT, we plotted the linear relationship of HgT<sub>UNF</sub> *versus* AOU, with the intercept  
397 at zero (mineralization curve, Fig. 5). The departure of the estimated HgT<sub>UNF</sub>  
398 concentrations for each SWT from the remineralization curve shows that, among the  
399 various SWTs, SAIW<sub>6</sub> and ENACW<sub>12</sub> exhibit Hg-enrichment, suggesting a significant  
400 control by hydrographical features. These two SWTs are within the upper layer (the top  
401 500 m), and thus more affected by atmospheric deposition. This observation suggests  
402 that direct atmospheric deposition would be a significant source of Hg in the upper NA  
403 waters, from the IrS to the ENAB. According to de Simone et al. (2016), anthropogenic  
404 Hg emissions contribute 20–25 % to present-day Hg deposition, two-thirds of which is  
405 deposited to the sea surface.

406 In summary, the distribution pattern of HgT<sub>UNF</sub> along the GEOTRACES-GA01  
407 transect, modelled by mixing of SWTs (Fig. S3), stresses the importance of organic  
408 matter regeneration and hydrological processes in Hg distribution in the NA.

## 409 **5.2. Change in anthropogenic Hg in LSW**

410 Evidence for a decrease in the Hg anthropization in the NA waters can be obtained from  
411 the comparison of the present results with those obtained twenty years ago with similar  
412 clean sampling and analytical techniques. In a companion paper (Cossa et al., in press),  
413 we have already compared the present findings for the convection layer in the LS with



414 the results of the 1993 International Oceanographic Commission cruise (Mason et al.,  
415 1998). Between 1993 and 2014 the decrease in  $\text{HgT}_{\text{UNF}}$  concentrations would have been  
416 more than a factor of two ( $1.14 \pm 0.36 \text{ pmol L}^{-1}$  versus  $0.40 \pm 0.07 \text{ pmol L}^{-1}$ ). An  
417 estimation of the anthropogenic Hg ( $\text{Hg}_{\text{Anth}}$ ) concentrations in subsurface waters can be  
418 inferred from the difference between measured  $\text{HgT}_{\text{UNF}}$  concentrations and the  
419 concentrations predicted based on a worldwide relationship between deep ocean Hg  
420 concentrations and remineralised phosphate (Lamborg et al., 2014), with a Redfield  
421 ratio of 141 between AOU and remineralized phosphate (Minster and Boulahdid, 1987)  
422 a more representative value for the North Atlantic than the global value of 170 proposed  
423 by Anderson and Sarmiento (1994). The LSWs take less than 20 years (Doney et al.,  
424 1997) to flow eastward more than 3000 km from the LS eastward to the Subtropical  
425 Gyre of the NA. Along its path, LSW bears the record of Hg solubility pumping at the  
426 time of their formation, thus sampling along its flow path allows the observation of  
427 decadal variations in anthropogenic Hg inputs to the NA. In the NA, estimation of  
428  $\text{Hg}_{\text{Anth}}$  concentrations in the core of LSW, defined within potential density of 27.74 and  
429 27.82, account for  $36 \pm 0.07 \%$  of the  $\text{HgT}_{\text{UNF}}$ , and are one third lower for younger  
430 waters (LS and IrS:  $0.16 \pm 0.11 \text{ pM}$ , mean  $\pm 1 \sigma$ ) than for older waters (IcB and ENAB:  
431  $0.24 \pm 0.06 \text{ pM}$ , mean  $\pm 1 \sigma$ ) (*t-test*,  $p < 0.01$ ; Fig. 6). Therefore, the observations of a  
432 temporal decrease of  $\text{Hg}_{\text{Anth}}$  in the marine boundary layer of the NA (Sprovieri et al.,  
433 2010; Soerensen et al., 2012; Weigelt et al., 2014) and 50%-loss of  $\text{Hg}_{\text{Anth}}$   
434 concentrations in the LSW over the last two decades are consistent. This means that  
435 LSW formed in the 1990s' in the LS, and currently present in the ENAB, received more  
436  $\text{Hg}_{\text{Anth}}$  from the atmosphere than the LSW<sub>2014-2015</sub> "vintage". These results contrast with



437 what can be deduced from the vertical profile of  $\text{HgT}_{\text{UNF}}$  in the LS, where the Hg  
438 regeneration in the water column is sufficient to account for the Hg increase between  
439 the shallow LSW layer ( $\text{LSW}_{2014-15}$ ) and the deep LSW layer ( $\text{LSW}_{1987-94}$ ) (Cossa et al.,  
440 in press). This discrepancy between these two deductions suggests that LSW, which are  
441 present in the Eastern NA, is likely older (and more imprinted by legacy  $\text{Hg}_{\text{Anth}}$ ) than  
442 the LSW currently present in the LS.

443 Nonetheless, the decrease in  $\text{HgT}_{\text{UNF}}$  in the NA is independently evidenced by the  
444 current observations compared with data collected in 1993 and 1994, in both Subpolar  
445 and Subtropical gyres, respectively (Mason et al., 1998; Cossa et al., 2004). In the  
446 Subpolar Gyre, at that time, the Hg concentration in the LSWs layers ranged from 0.55  
447 to 1.64  $\text{pmol L}^{-1}$ . In the Subtropical Gyre, a multipeak pattern was also observed in 1994  
448 in the Eastern Atlantic slope water column in the Celtic Sea (Cossa et al., 2004). The  
449 shape of the Hg profiles exhibited the same peaks in the same water masses as the ones  
450 observed in this study (i.e., SPMW and MW). However,  $\text{HgT}_{\text{UNF}}$  concentration levels,  
451 measured 20 years ago, were much higher varying mostly often from 0.3  $\text{pmol L}^{-1}$  in  
452 sub-surface waters to more than 2.0  $\text{pmol L}^{-1}$  at depth. A decrease in HgT  
453 concentrations over the last three decades supports the estimated decline in Hg  
454 concentrations in subsurface waters of the NA estimated by models (e.g., Soerensen et  
455 al., 2012).

### 456 **5.3. Latitudinal transport of Hg**

457 The transport of  $\text{HgT}_{\text{UNF}}$  per unit of water mass, calculated with Eq. (2) (Material and  
458 Methods section), are given in Table 2. We also applied Eq. (2) separately to the upper  
459 and lower limbs of the AMOC and computed the transports of  $\text{HgT}_{\text{UNF}}$  per water mass



460 for the two limbs. The velocity fields across the Portugal-Greenland transect was  
461 calculated using inverse model constrained by Doppler current profiler velocity  
462 measurements (Zunino et al., this issue). The volume transport per SWT was computed  
463 by combining this velocity fields with the results of the eOMP (García-Ibáñez et al., this  
464 issue).

465       There is a northward  $HgT_{UNF}$  transport within the upper limb of the AMOC (10.8  
466  $mmol s^{-1}$ ), and a southward  $HgT_{UNF}$  transport within the lower limb ( $7.3 mmol s^{-1}$ ).  
467 Most of the  $HgT_{UNF}$  southward transport is due to IrSPMW and PIW displacements,  
468 whereas  $HgT_{UNF}$  northward transport is associated with ENACW<sub>12</sub> and SPMW<sub>8</sub>  
469 displacements. In addition, the mean (velocity-weighted)  $HgT_{UNF}$  concentration of the  
470 water advected northwards within the upper limb of the AMOC ( $0.58 pmol L^{-1}$ ) is  
471 higher than the one advected southwards within the lower limb of the AMOC ( $0.42$   
472  $pmol L^{-1}$ ). Thus, across the Portugal-Greenland transect, there is a net transport of 111  
473  $kmol yr^{-1}$  from mid-latitudes to polar zones. To be able to estimate the Hg exchange  
474 between Arctic Ocean and NA, the LS section has to be taken into account. The Hg  
475 transport associated with the LC can be roughly estimated at  $133 kmol yr^{-1}$ , using the  
476 mean southward water transport of the shelf edge LC is at the Seal Island transect  
477 (Hamilton Bank near Stas. 77 and 78) which is 7.5 Sv, according to Han et al. (2008)  
478 and a mean  $HgT$  concentration of  $0.56 pmol L^{-1}$  (Cossa et al., in press). Thus, as a first  
479 approximation, the net Hg exchange between the Arctic Ocean and NA would be an  
480 Arctic loss of  $22 kmol yr^{-1}$ , a smaller value than the estimate ( $130 kmol yr^{-1}$ ) proposed  
481 by the budget recently built by Soerensen et al. (2016).

482

483 **6. Summary and conclusions**

484  $\text{HgT}_{\text{UNF}}$  concentrations in the waters along the GEOTRACES-GA01 transect, which  
485 crossed the NA from 40°N to 60°N (Portugal to Canada), ranged from 0.16 to 1.54  
486  $\text{pmol L}^{-1}$ , but with 97 % lower than 1.00  $\text{pmol L}^{-1}$  and a geometric mean of 0.51  $\text{pmol L}^{-1}$   
487 ( $n = 535$ ). Below 100 m, most of  $\text{HgT}_{\text{UNF}}$  (62-98%) is present as dissolved species (<  
488 45  $\mu\text{m}$ ).  $\text{HgT}_{\text{UNF}}$  concentrations increased eastwards and downwards, with the highest  
489  $\text{HgT}_{\text{UNF}}$  concentrations found in the Subtropical Gyre, and especially within NEADW<sub>L</sub>.  
490 The relationship between  $\text{HgT}_{\text{F}}$  and AOU reflects organic matter regeneration processes  
491 on  $\text{HgT}$  mobilization and confirms a nutrient-like behavior for Hg in the NA. Using the  
492  $\text{HgT}_{\text{UNF}}$  fraction unexplained by regeneration processes as a proxy for  $\text{Hg}_{\text{Anth}}$ , we  
493 observed geographical and temporal trends in the  $\text{Hg}_{\text{Anth}}$  in the NA. First, the highest  
494 proportions of  $\text{Hg}_{\text{Anth}}$  were found in the upper layer of the eastern NA (ENACW<sub>12</sub> and  
495 SPMW<sub>8</sub>). Secondly, there is an eastward increase within LSW, which suggests that Hg  
496 incorporation in the downwelling waters of the LS has decreased over the last 20 years,  
497 in parallel with the decrease of Hg concentrations in the NA troposphere. A net  
498 northward Hg transfer of 111  $\text{kmol yr}^{-1}$  across the Portugal-Greenland transect results of  
499 the AMOC. Taking into account the southern Hg export with the LC, the net Hg  
500 exchange between the Arctic Ocean and NA would be an Arctic loss of 22  $\text{kmol yr}^{-1}$ .

501

502 **Abbreviations:** AABW, Antarctic Bottom Water; AFS, atomic fluorescence  
503 spectrometer; AMOC, Atlantic Meridional Oceanic Circulation; AOU, Apparent  
504 Oxygen Utilization; CFCs, chlorofluorocarbons; CRM, certified reference material; DL,  
505 detection limit; DSOW, Denmark Strait Overflow Water; DWBC, Deep Western  
506 Boundary Current; EGC, Eastern Greenland Current; ENAB, Eastern North Atlantic  
507 basin; ENACW, East North Atlantic Central Water; eOMP, extended Optimum  
508 Multiparameter analysis; Hg, mercury;  $\text{HgT}_{\text{Anth}}$ , anthropogenic  $\text{HgT}$ ;  $\text{HgT}$ , total  
509 mercury;  $\text{HgT}_{\text{UNF}}$ , unfiltered  $\text{HgT}$ ;  $\text{HgT}_{\text{F}}$ , filtered  $\text{HgT}$ ; IAP, Iberian abyssal plain; ICB,



510 Iceland basin; IOC, International Oceanographic Commission; IrS, Irminger Sea;  
511 ISOW, Iceland-Scotland Overflow Water; LC, Labrador Current; LS, Labrador Sea;  
512 LSW, Labrador Sea Water; MW, Mediterranean Water; NA, North Atlantic Ocean;  
513 NAC, North Atlantic Current; NADW, North Atlantic Deep Water; NEADW<sub>L</sub>, Lower  
514 North East Atlantic Deep Water ; PIW, Polar Intermediate Water; SPMW, Subpolar  
515 Mode Water; SWT, Source Water Type; WGC, Western Greenland Current.

516

517 **Acknowledgments:** The first thanks are for J. Boutorh, M. Cheize, J.-L. Menzel and R.  
518 Shelley who were in charge of the ultra-trace sampling organization; they are  
519 commended for its successful achievement. Thanks are also due to other members of the  
520 GEOVIDE team for participating to data acquisition: F. Alonso Pérez, R. Barkhouse, V.  
521 Bouvier, P. Branellec, L. Carracedo Segade, M. Castrillejo, L. Contreira, N. Deniault, F.  
522 Desprez de Gesincourt, L. Foliot, D. Fonseca Pereira, E. Grossteffan, P. Hamon, C.  
523 Jeandel, C. Kermabon, F. Lacan, P. Le Bot, M. Le Goff, A. Lefebvre, S. Leizour, N.  
524 Lemaitre, O. Menage, F. Planchon, A. Roukaerts, V. Sanial, R. Sauzède, and Y. Tang.  
525 A special thank is also due to the R/V “*Pourquoi Pas?*” crew and Captain G. Ferrand,  
526 and the DT INSU (E. de Saint Léger, F. Pérault) who organized the rosette  
527 deployment/recovery processes. This research was founded by the French National  
528 Research Agency (ANR-13-BS06-0014, ANR-12-PDOC-0025-01), the French National  
529 Center for Scientific Research (CNRS-LEFE-CYBER), the LabexMER (ANR-10-LABX-  
530 19), the Global Mercury Observation System (GMOS, N°265113 European Union  
531 project), and the European Research Council (ERC-2010-StG-20091028). For this work  
532 M.I. García-Ibáñez and F.F. Pérez were supported by the Spanish Ministry of Economy  
533 and Competitiveness through the BOCATS (CTM2013-41048-P) project co-funded by  
534 the Fondo Europeo de Desarrollo Regional 2014-2020 (FEDER).

535

536

537

538

## 539 References

540 Amos, H. M., J. E. Sonke, J. E., Obrist, D., Robins, N., Hagan, N., Horowitz, H. M.,

541 Mason, R. P., Witt, M., Hedgecock, I. M., Corbitt, E. S., and Sunderland, E. M.:

542 Observational and Modeling Constraints on Global Anthropogenic Enrichment of

543 Mercury. *Environ. Sci. Technol.*, 49, 4036-4047, 2015.

544 Anderson, L. A., and Sarmiento, J. L.: Redfield ratios of remineralization determined by

545 nutrient data-analysis. *Glob. Biogeochem. Cycles*, 8, 65–80, 1994.

546 Azetsu-Scott, K., Jones, E.P., Yashayaev, I., Gershey, R.M. 2003. Time series study of

547 CFC concentrations in the Labrador Sea during deep and shallow convection regimes

548 (1991–2000). *J. Geophys. Res.*, 108 (C11), 3354.



- 549 Bloom, N. S., and Crecelius, E. A.: Determination of mercury in seawater at sub-  
550 nanogram per liter levels, *Mar. Chem.*, 14, 49–59, doi:10.1016/0304-4203(83)90069-5,  
551 1985.
- 552 Bowman, K. L., Hammerschmidt, C. R., Lamborg, C. H., and Swarr, G. J.:  
553 Mercury in the North Atlantic Ocean: The U.S. GEOTRACES zonal and  
554 meridional, *Deep Sea Res. Part II*, 116, 251–261, doi:10.1016/j.dsr2.2014.07.004,  
555 2015.
- 556 Brambilla, E., and Talley, L. D.: Subpolar Mode Water in the northeastern Atlantic: 1.  
557 Averaged properties and mean circulation, *J. Geophys. Res., Oceans*, 113(C4), C04025,  
558 doi:10.1029/2006JC004062, 2008.
- 559 Bratkič, A., Vahčić, M., Kotnik, J., Obu Vazner, K., Begu, E., Woodward, E. M. S., and  
560 Horvat, M.: Mercury presence and speciation in the South Atlantic Ocean along the  
561 40°S transect, *Global Biogeochem. Cycles*, 30, 105–119, doi:10.1002/2015GB005275,  
562 2016.
- 563 Bratkič, A.: Chemistry Department, Vrije Universiteit Brussel, Pleinlaan 2, 1050  
564 Brussels, Belgium. Email: arne.bratkic@vub.ac.be.
- 565 Cianca A., Santana, R., Marrero, J. P., Rueda, M. J., and Llina, O.: Modal composition  
566 of the central water in the North Atlantic subtropical gyre, *Ocean Sci. Discuss.*, 6,  
567 2487–2506, doi:10.5194/osd-6-2487-2009, 2009.
- 568 Cossa, D., and Courau, P.: An international intercomparison exercise for total mercury  
569 in seawater, *Appl. Organometal. Chem.*, 4, 49–54, doi:10.1002/aoc.590040109, 1990.
- 570 Cossa, D., and Coquery, M.: The Mediterranean mercury anomaly, a geochemical or a  
571 biological issue. pp 177-208. In: *The Mediterranean Sea*. Handbook of Environmental  
572 Chemistry, Vol 5. Salot, A. editor. Springer, 413 p. 2005. ISSN 1433-6863, 2005.
- 573 Cossa D., Cotté-Krief M.-H., Mason R. P., and Bretaudeau-Sanjuan J.: Total mercury in  
574 the water column near the shelf edge of the European continental margin, *Mar. Chem.*,  
575 90, 21–29, doi:10.1016/j.marchem.2004.02.019, 2004.



- 576 Cossa, D., Heimbürger, L.-E., Lannuzel, D., Rintoul, S. R., Butler, E. C. V., Bowie, A.  
577 R., Averty, B., Watson, R. J., Remenyi, T.: Mercury in the Southern Ocean. *Geochim.*  
578 *Cosmochim. Acta*, 7, 4037–4052, doi:10.1016/j.gca.2011.05.001, 2011.
- 579 Cossa, D., Durrieu de Madron, X., Schäfer, J., Guédron, S., Maruszczak, N., Castelle, S.,  
580 and Naudin, J.-J.: Sources and exchanges of mercury in the waters of the Northwestern  
581 Mediterranean margin, *Prog. Oceanogr.* doi.org/10.1016/j.pocean.2017.05.002, 2017.
- 582 Cossa, D., L.-E. Heimbürger, L.-E., Sonke, J. E., Planquette, H., Lherminier, P., García-  
583 Ibáñez, M. I., Pérez, F. F., and Sarthou, G.: Sources, recycling and transfer of mercury  
584 in the Labrador Sea (GEOTRACES-GEOVIDE cruise). *Mar. Chem.*, in press.
- 585 Cutter, G. A., and Bruland, K. W.: Rapid and noncontaminating sampling system for  
586 trace elements in global ocean surveys. *Limnol. Oceanogr. - Methods* 10, 425–436,  
587 doi:10.4319/lom.2012.10.425, 2012.
- 588 Cutter, G., Casciotti, K., Croot, P., Geibert, W., Heimbürger, L. E., Lohan, M.,  
589 Planquette, H., and van de Fliert, T.: GEOTRACES cookbook: Sampling and sample-  
590 handling protocols for GEOTRACES cruises. Version 3, edited by the 2017 GEOTRACES  
591 Standards and Intercalibration Committee: Version 3.0; August 2017.
- 592 Daniault, N., Lherminier, P., and Mercier, H.: Circulation and transport at the southeast  
593 tip of Greenland, *J. Phys. Oceanogr.*, 41, 437–457, doi:10.1175/2010JPO4428.1, 2011.
- 594 Daniault, N., Mercier, H., Lherminier, P., Sarafanov, A., Falina, A., Zunino, P., Pérez,  
595 F. F., Ríos, A. F., Ferron, B., Huck, T., Thierry, V., and Gladyshev, S.: The northern  
596 North Atlantic Ocean mean circulation in the early 21st century, *Progr. Oceanogr.*, 146,  
597 142–158, doi:10.1016/j.pocean.2016.06.007, 2016.
- 598 de la Paz, M., García-Ibáñez, M. I., Steinfeldt, R., Ríos, A. F., and Pérez F. F.:  
599 Ventilation versus biology: What is the controlling mechanism of nitrous oxide  
600 distribution in the North Atlantic?, *Global Biogeochem. Cycles*, 31, 745–760,  
601 doi:10.1002/2016GB005507, 2017.
- 602 de Simone, F., Gencarelli, C. N., Hedgecock, I. M., and Pirrone, N.: A Modeling  
603 Comparison of Mercury Deposition from current Anthropogenic Mercury Emission  
604 Inventories, *Environ. Sci. Technol.*, 50, 5154–5162, doi:10.1021/acs.est.6b00691, 2016.



- 605 Doney, S. C., Jenkins, W. J., and Bullister, J. L.: A comparison of ocean tracer dating  
606 techniques on a meridional section in the eastern North Atlantic. *Deep Sea Res. I*, 44,  
607 603–626, 1997.
- 608 EPA (Environmental Protection Agency, US): Method 1631, Revision E: Mercury in  
609 water by oxidation, purge and trap, and cold vapor atomic fluorescence spectrometry.  
610 EPA-821-R-02-019, 2002. [http://water.epa.gov/scitech/methods/cwa/metals/mercury/  
611 index.cfm](http://water.epa.gov/scitech/methods/cwa/metals/mercury/index.cfm), 2002.
- 612 Fitzgerald, W. F., Lamborg, C. H., and Hammerschmidt, C. R.: Marine biogeochemical  
613 cycling of mercury. *Chem. Rev.*, 107, 641–662, 2007.
- 614 Fontela, M., García-Ibáñez, M. I., Hansell, D. A., Mercier, H., and Pérez, F. F.:  
615 Dissolved Organic Carbon in the North Atlantic Meridional Overturning Circulation,  
616 *Sci. Rep.*, 6, 26931, doi:10.1038/srep26931, 2016.
- 617 García-Ibáñez, M. I., Pardo, P. C., Carracedo, L. I., Mercier, H., Lherminier, P., Rios,  
618 A. F., and Pérez, F. F.: Structure, transports and transformations of the water masses in  
619 the Atlantic Subpolar Gyre, *Prog. Oceanogr.*, 135, 18–36, doi:10.1016/j.pocean.2015.  
620 03.009, 2015.
- 621 García-Ibáñez, M. I., Pérez, F. F., Lherminier, P., Zunino, P., and Treguer, P.: Water  
622 mass distributions and transports for the 2014 GEOVIDE cruise in the North Atlantic.  
623 This issue.
- 624 Gill, G. A., and Fitzgerald, W. F.: Mercury sampling of open ocean waters at the  
625 picomolar level, *Deep Sea Res. Part A*, 32, 287–297, doi:10.1016/0198-0149(85)90080-  
626 9, 1985.
- 627 Gourcuff, C., Lherminier, P., Mercier, H., and Le Traon, P. Y.: Altimetry combined  
628 with hydrography for ocean transport estimation, *J. Atmos. Oceanogr. Technol.*, 28,  
629 1324–1337, doi:10.1175/2011JTECHO818.1, 2011.
- 630 Han, G., Lu, Z. Wang, Z., Helbig, J., Chen, N., and de Young, B.: Seasonal variability  
631 of the Labrador Current and shelf circulation off Newfoundland, *J. Geophys. Res.*, 113,  
632 C10013, doi:10.1029/2007JC004376, 2008.



- 633 Heimbürger, L.-E., Sonke, J., Cossa, D., Point, D., Lagane, C., Laffont, L., Galfond, B.  
634 T., Nicolaus, M., Rabe, B., and Rutgers van der Loeff, M.: Shallow methylmercury  
635 production in the marginal sea ice zone of the central Arctic Ocean, *Sci. Rep.*, 5, 10318,  
636 doi:10.1038/srep10318, 2015.
- 637 Hewitt, C. N.: *Instrumental Analysis of Pollutants*. Elsevier Applied Science, 1989.
- 638 Lamborg, C. H., Hammerschmidt, C. R., Gill, G. A., Mason, R. P., and Gichuki, S.: An  
639 intercomparison of procedures for the determination of total mercury in seawater and  
640 recommendations regarding mercury speciation during GEOTRACES cruises, *Limnol.*  
641 *Oceanogr. – Methods*, 10, 90–100, doi:10.4319/lom.2012.10.90, 2012.
- 642 Lamborg, C. H., Hammerschmidt C. R., Bowman, K. L., Swarr, G. J., Munson, K. M.,  
643 Ohnemus, D. C., Lam, P. J., Heimbürger, L.-E., Rijkenberg, M. J. A., and Saito, M. A.:  
644 A global ocean inventory of anthropogenic mercury based on water column measurements,  
645 *Nature*, 512, 65–68, doi:10.1038/nature13563, 2014.
- 646 Lherminier, P., Mercier, H., Gourcuff, C., Álvarez, M. F., Bacon, S., and Kermabon, C.:  
647 Transport across the 2002 Greenland-Portugal section and comparison with 1997, *J.*  
648 *Geophys. Res.*, 112(C07003), doi:10.1029/2006JC003716, 2007.
- 649 Lherminier, P., Mercier, H., Huck, T., Gourcuff, C., Pérez, F. F., Morin, P., Sarafanov,  
650 A., and Falina, A.: The Atlantic Meridional Overturning Circulation and the Subpolar  
651 Gyre observed at the A25-OVIDE Section in June 2002 and 2004, *Deep-Sea Res.*, I, 57,  
652 1374–1391, doi:10.1016/j.dsr.2010.07.009, 2010.
- 653 McCartney, M. S.: Recirculating components to the deep boundary current of the  
654 northern North Atlantic, *Prog. Oceanogr.*, 29, 283–383, doi:10.1016/0079-  
655 6611(92)90006-L, 1992.
- 656 McCartney, M. S., and Talley, L. D.: The subpolar mode water of the North Atlantic  
657 Ocean, *J. Phys. Oceanogr.*, 12, 1169–1188, doi:10.1175/1520-0485(1982)  
658 012<1169:TSMWOT>2.0.CO;2, 1982.
- 659 McCartney, M. S., and Talley, L. D.: Warm-to-cold conversion in the northern North  
660 Atlantic Ocean, *J. Phys. Oceanogr.*, 14, 922–935, doi:10.1175/1520-  
661 0485(1984)014<0922:WTCWCI>2.0.CO;2, 1984.



- 662 Mason, R.P., Choi, A.L., Fitzgerald, W.F., Hammerschmidt, C.R., Lamborg, C.H.,  
663 Soerensen, A.L., and Sunderland, E.M.: Mercury biogeochemical cycling in the ocean  
664 and policy implications. *Environ. Res.* 119, 101–117, 2012.
- 665 Mason R. P., Rolfus K. R., and Fitzgerald W. F.: Mercury in the North Atlantic, *Mar.*  
666 *Chem.*, 61, 37–53, doi:10.1016/S0304-4203(98)00006-1, 1998.
- 667 Mercier, H., Lherminier, P., Sarafanov, A., Gaillard, F., Daniault, N., Desbruyères, D.,  
668 Falina, A., Ferron, B., Gourcuff, C., Huck, T., and Thierry, V.: Variability of the  
669 meridional overturning circulation at the Greenland-Portugal OVIDE section from 1993  
670 to 2010, *Prog. Oceanogr.*, 132, 250–261, doi:10.1016/j.pocean.2013.11.001, 2015.
- 671 Minster, J.-F., and Boulahdid, M.: Redfield ratios along isopycnal surfaces---a  
672 complementary study. *Deep Sea Res.*, 34, 1981-2003, 1987.
- 673 Morel, F. M. M., Milligan, A. J., and M. A. Saito, M. A.: Marine Bioinorganic  
674 Chemistry: The Role of Trace Metals in the Oceanic Cycles of Major Nutrients. *Treatise*  
675 *on Geochemistry*, Holland, H. D. and Turekian, K. K. editors, Volume 6, 113-143,  
676 2003.
- 677 Munson, K. M., Lamborg, C. H., Swarr, G. J., and Saito, M. A.: Mercury species  
678 concentrations and fluxes in the Central Tropical Pacific Ocean, *Global Biogeochem.*  
679 *Cycles*, 29, 656–676, doi:10.1002/2015GB005120, 2015.
- 680 Pickart, R. S., Straneo, F., and Moore, G. K.: 2003. Is Labrador Sea Water formed in the  
681 Irminger basin? *Deep Sea Res. Part I*, 50, 23-52, doi: 1180 10.1016/S0967-  
682 0637(02)00134-6, 2003.
- 683 Pirrone, N., and Mahaffey, K. R.: *Dynamics of Mercury Pollution on Regional and*  
684 *Global Scales*, Springer Publishers, New York, p 744, 2005.
- 685 Rhein, M., Fisher, J., Smethie, W. M., Smythe-Wright, D., Weiss, R. F., Mertens, C.,  
686 Min, D.-H., Fleischmann, U., and Putzka, A.: Labrador Sea water: Pathways, CFC  
687 Inventory, and Formation Rates, *J. Phys. Oceanogr.*, 32, 648–665, doi:10.1175/1520-  
688 0485(2002)032<0648:LSWPCI>2.0.CO;2, 2002.



- 689 Smethie, W. M., Fine, R. A., Putzka, A., and Jones, E. P.: Tracing the flow of North  
690 Atlantic Deep Water using chlorofluorocarbons, *J. Geophys. Res.*, 105, 14297–14323,  
691 doi:10.1029/1999JC900274, 2000.
- 692 Soerensen, A. L., Jacob, D. J., Streets, D. G., Witt, M. L. I., Ebinghaus, R., Mason, R.  
693 P., Andersson, M., and Sunderland, E. M.: Multi-decadal decline of mercury in the  
694 North Atlantic atmosphere explained by changing subsurface seawater concentrations,  
695 *Geophys. Res. Lett.*, 39, L21810, doi:10.1029/2012GL053736, 2012.
- 696 Soerensen, A. L., Jacob, D. J., Schartup, A. T., Fisher, J. A., Lehnherr, I., St. Louis, V.  
697 L., Heimbürger, L. E., Sonke, J. E., Krabbenhoft, D. P., and Sunderland, E. M.: A mass  
698 budget for mercury and methylmercury in the Arctic Ocean, *Global Biogeochem.*  
699 *Cycles*, 30, doi:10.1002/2015GB005280, 2016.
- 700 Sonke, J. E., Heimbürger, L.-E., and Dommergue, A.: Mercury biogeochemistry:  
701 Paradigm shifts, outstanding issues and research needs. *CR Geosci.*, 345, 213–224,  
702 2013.
- 703 Sprovieri, F., Pirrone, N., Ebinghaus, R., Kock, H., and Dommergue, A.: A review of  
704 worldwide atmospheric mercury measurements, *Atmos. Chem. Phys.*, 10, 8245–8265,  
705 doi:10.5194/acp-10-8245-2010, 2010.
- 706 Taylor, J. K.: *Quality Assurance of Chemical Measurements*. Lewis Publishers, 1987.
- 707 Tsuchiya, M., Talley, L. D., and McCartney, M. S.: An eastern Atlantic section from  
708 Iceland southward across the equator, *Deep Sea Res. Part A*, 39, 1885–1917,  
709 doi:10.1016/0198-0149(92)90004-D, 1992.
- 710 UNEP.: <http://mercuryconvention.org>, 2013.
- 711 van Aken, H. M., and Becker, G.: Hydrography and through-flow in the northeastern  
712 North Atlantic Ocean: the NANSEN project, *Progr. Oceanogr.* 38, 297–346,  
713 doi:10.1016/S0079-6611(97)00005-0, 1996.
- 714 Weigelt, A., Ebinghaus, R., Manning, A. J., Derwent, R. G., Simmonds, P. G., Spain, T.  
715 G., Jennings, S. G., and Slemr, F.: Analysis and Interpretation of 18 years of mercury  
716 observations since 1996 at Mace Head, Ireland, *Atmos. Environ.*, 100, 85–93,  
717 doi:10.1016/j.atmosenv.2014.10.050, 2014.



- 718 Yashayaev, I., and Loder, J. W.: Recurrent replenishment of Labrador Sea Water and  
719 associated decadal-scale variability, *J. Geophys. Res. Oceans*, 121, 8095–8114,  
720 doi:10.1002/2016JC012046, 2016.
- 721 Zunino, P., Lherminier, P., Mercier, H., Daniault, N., García-Ibáñez, M. I., and Pérez, F.  
722 F.: The GEOVIDE cruise in May-June 2014 revealed an intense MOC over a cold and  
723 fresh subpolar North Atlantic. This issue.
- 724



725 **Figure caption**

726 **Figure 1.** Schematic view of the water circulation in the North Atlantic Ocean adapted  
727 from García-Ibáñez et al. (2015) and Danialt et al. (2016). Red lines indicate the  
728 circulation in surface, while blue lines indicated circulation at depth. Black lines  
729 represent the GEOVIDE cruise transects (GEOTRACES-GA01). Main geographical  
730 features, water masses and currents are indicated: Newfoundland (NFL), United  
731 Kingdom (U.K.), United States of America (U.S.A.); Denmark Strait Overflow Water  
732 (DSOW), Iceland-Scotland Overflow water (ISOW), Labrador Sea Water (LSW),  
733 Lower North East Atlantic Deep water (NEADW<sub>L</sub>), Mediterranean Water (MW), and  
734 North Atlantic Deep Water (NADW), Deep Western Boundary Current (DWBC),  
735 Eastern Greenland Current (EGC), Labrador Current (LC), North Atlantic Current  
736 (NAC), Western Greenland Current (WGC).

737 **Figure 2.** Distribution of unfiltered total mercury ( $\text{HgT}_{\text{UNF}}$ ) concentrations along the  
738 GEOTRACES-GA01 transect. LS: Labrador Sea; IrS: Irminger Sea; IcB: Iceland basin;  
739 ENABw: west part of Eastern North Atlantic basin; ENABe: east part of Eastern North  
740 Atlantic basin; IAP: Iberian Abyssal Plain.

741 **Figure 3.** Mercury concentrations in filtered ( $\text{HgT}_{\text{F}}$ ) vs unfiltered ( $\text{HgT}_{\text{UNF}}$ ) samples ( $n$   
742 = 141) collected along the GEOTRACES-GA01 transect.

743 **Figure 4.** Total Hg in filtered samples ( $\text{HgT}_{\text{F}}$ ) vs apparent oxygen utilization (AOU)  
744 relationship along the GEOTRACES-GA01 transect.

745 **Figure 5.** Total Hg in unfiltered samples ( $\text{HgT}_{\text{UNF}}$ ) vs apparent oxygen utilization  
746 (AOU) relationship within the various Source Water Types.

747 **Figure 6.** Anthropogenic HgT ( $\text{HgT}_{\text{Anth}}$ ) concentration distribution in the core of the  
748 Labrador Sea Water (LSW) ( $S = 34.9$ ,  $\sigma_{\theta} = 27.74\text{--}27.82$ , 1200–2000 m) between the  
749 Labrador Sea and the Eastern North Atlantic basin.  $\text{HgT}_{\text{Anth}}$  values were obtained  
750 according to the model by Lamborg et al. (2014). Young LSW corresponds to the  
751 “2014-vintage” (LSW<sub>2014</sub>) formed during winter 2013–2014. The insert shows the Hg  
752 concentration decrease in the troposphere over the North Atlantic during the last 20  
753 years according to Soerensen et al. (2012).

754 **Tables**

755

756 **Table 1.** Total Hg in unfiltered samples ( $\text{HgT}_{\text{UNF}}$ ) vs apparent oxygen utilization (AOU)  
 757 concentrations of each source water type (SWT), calculated according to eOMP (Eq. 1)  
 758 (see also García-Ibáñez et al., this issue). ENACW<sub>12</sub>: East North Atlantic Central Water of  
 759 12°C; SPMW<sub>8</sub> and SPMW<sub>7</sub>: Subpolar Mode Waters of the Iceland basin of 7 and 8°C;  
 760 IrSPMW: Subpolar Mode Water of the Irminger basin; LSW: Labrador Sea Water; MW:  
 761 Mediterranean Water; ISOW: Iceland-Scotland Overflow Water; NEADW<sub>L</sub>: lower North  
 762 East Atlantic Deep Water; DSOW: Denmark Strait Overflow Water; PIW: Polar  
 763 Intermediate Water; and SAIW<sub>6</sub>: Subarctic Intermediate Water of 6°C.

SWT	$\text{HgT}_{\text{UNF}}$ (pmol L <sup>-1</sup> )	AOU (μmol L <sup>-1</sup> )
ENACW <sub>12</sub>	0.47 ± 0.01	13.4 ± 1.3
SPMW <sub>8</sub>	0.77 ± 0.03	112.8 ± 3.1
SPMW <sub>7</sub>	0.54 ± 0.03	65.4 ± 2.7
IrSPMW	0.26 ± 0.03	20.8 ± 2.7
LSW	0.46 ± 0.01	37.6 ± 1.0
MW	0.75 ± 0.04	84.7 ± 4.3
ISOW	0.59 ± 0.02	53.3 ± 2.2
NEADW <sub>L</sub>	1.02 ± 0.02	98.6 ± 2.0
DSOW	0.43 ± 0.03	32.0 ± 3.0
PIW	0.73 ± 0.11	77.3 ± 10.8
SAIW <sub>6</sub>	0.45 ± 0.03	-12.7 ± 3.0

764

765



766 **Table 2.** Water and total Hg in unfiltered samples ( $\text{HgT}_{\text{UNF}}$ ) transport by the upper and  
 767 lower limbs of the Atlantic Meridional Overturning Circulation. Positive (negative)  
 768 transports correspond to northward (southward) flow.

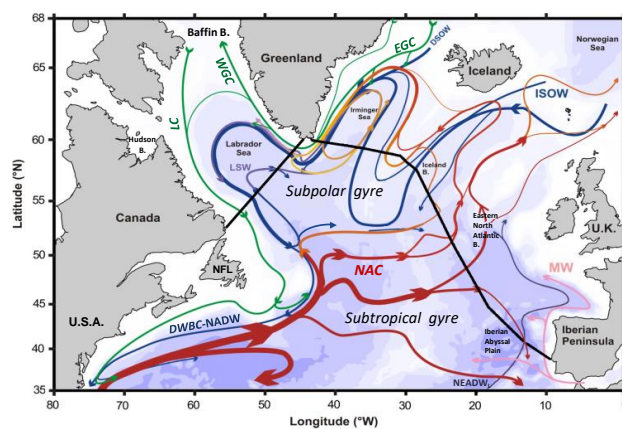
SWT	Entire water column		Upper limb		Lower limb	
	Water transport (Sv)	$\text{HgT}_{\text{UNF}}$ transport ( $\text{mmol s}^{-1}$ )	Water transport (Sv)	$\text{HgT}_{\text{UNF}}$ transport ( $\text{mmol s}^{-1}$ )	Water transport (Sv)	$\text{HgT}_{\text{UNF}}$ transport ( $\text{mmol s}^{-1}$ )
ENACW <sub>12</sub>	9.6	4.65	9.6	4.65	0.0	0.00
SPMW <sub>8</sub>	4.1	3.28	3.7	2.92	0.5	0.36
SPMW <sub>7</sub>	3.2	1.75	1.8	0.99	1.4	0.76
IrSPMW	-10.1	-2.73	-0.8	-0.22	-9.3	-2.51
LSW	1.5	0.70	2.7	1.31	-1.3	-0.60
MW	0.7	0.56	0.6	0.50	0.1	0.06
ISOW	0.9	0.55	1.2	0.76	-0.3	-0.21
NEADW <sub>L</sub>	0.3	0.33	0.0	0.00	0.3	0.33
DSOW	-2.2	-0.98	-0.1	-0.06	-2.1	-0.91
PIW	-4.8	-3.59	0.0	0.00	-4.8	-3.59
SAIW <sub>6</sub>	-2.1	-0.99	0.0	0.00	-2.1	-0.99
<b>TOTAL</b>	<b>1.1</b>	<b>3.52</b>	<b>18.7</b>	<b>10.84</b>	<b>-17.7</b>	<b>-7.32</b>

769

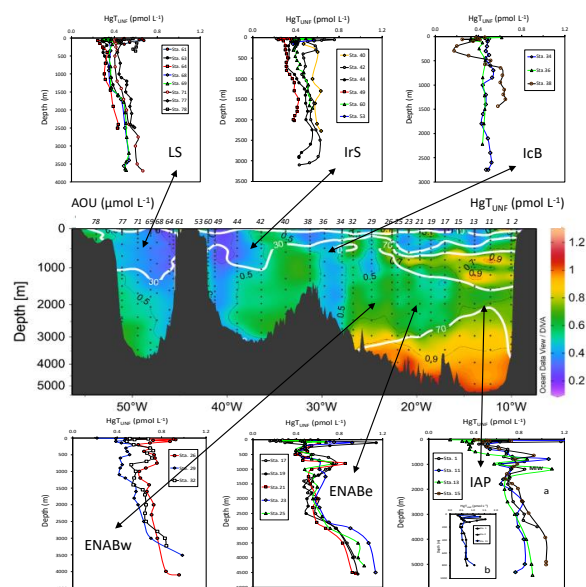
770



771



772 Fig. 1



773 Fig. 2

774

775

776



776

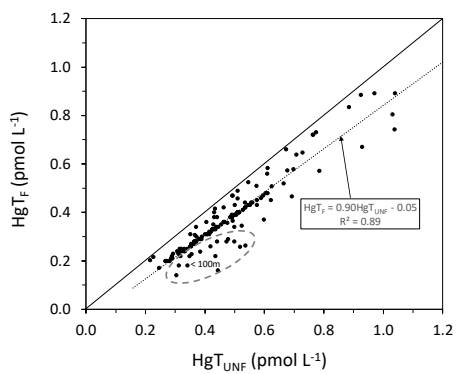


Fig. 3

777

778

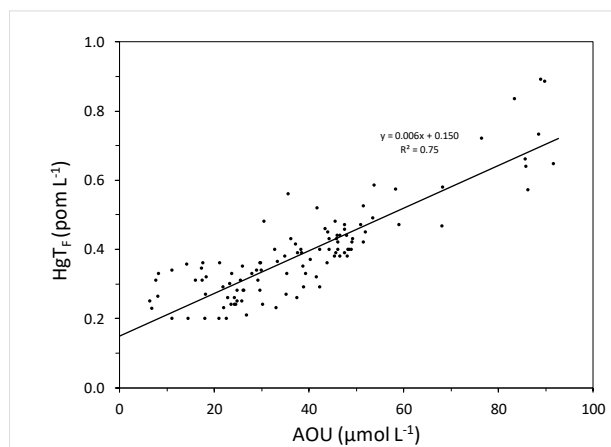


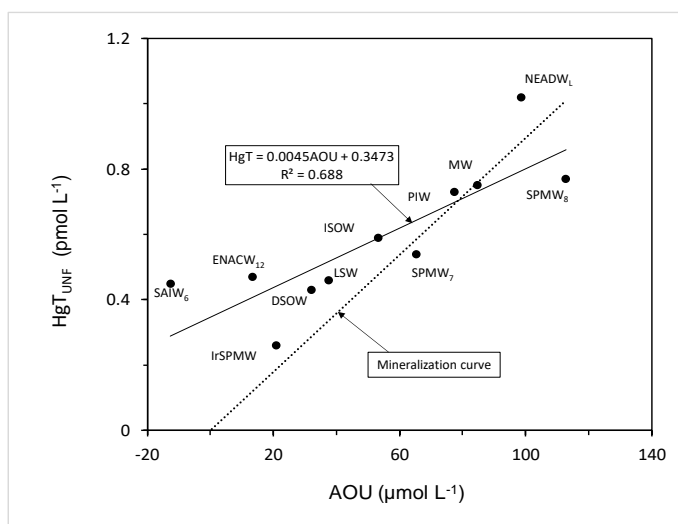
Fig. 4

779

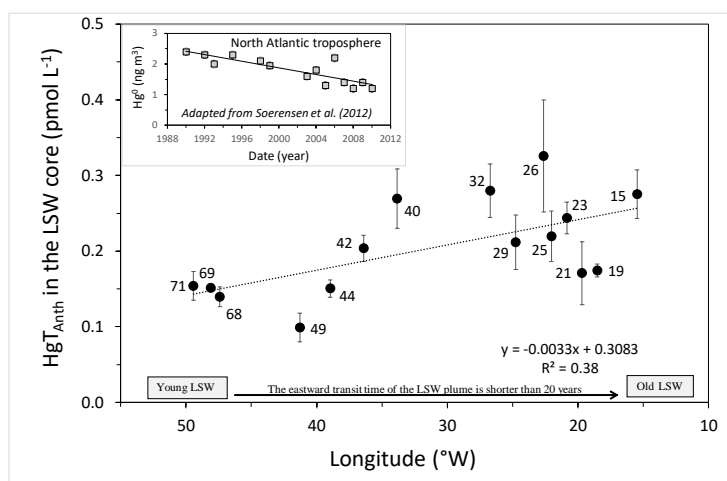
780



781



782 Fig. 5



783 Fig. 6

784